PAPER

Check for updates

New C_{2h} phase of group III monochalcogenide monolayers AlX (X = S, Se, and Te) with anisotropic crystal structure: first-principles study

Tuan-Anh Tran, [ID] [a] Le S. Hai,[a] Cuong Q. Nguyen, [ID] [bc] Vo T. T. Vi, [ID] [d] Tran P. T. Linh [ID] [e] and Nguyen N. Hieu [ID] *[bc]

In this paper, we introduce a new phase of two-dimensional aluminum monochalcogenide, namely C_{2h}-AlX (X = S, Se, and Te). With the C_{2h} space group, C_{2h}-AlX possesses a large unit cell containing 8 atoms. The C_{2h} phase of AlX monolayers is found to be dynamically and elastically stable based on the evaluation of its phonon dispersions and elastic constants. The anisotropic atomic structure of C_{2h}-AlX leads to a strong anisotropy in its mechanical properties with Young's modulus and Poisson's ratio strongly dependent on the directions examined in the two-dimensional plane. All three monolayers of C_{2h}-AlX are found to be direct band gap semiconductors, which are compared with the indirect band gap semiconductors of available D_{3h}-AlX. Particularly, the transition from direct to indirect band gap is observed in C_{2h}-AlX when a compressive biaxial strain is applied. Our calculated results indicate that C_{2h}-AlX exhibits anisotropic optical characteristics and its absorption coefficient is high. Our findings suggest that C_{2h}-AlX monolayers are suitable for applications in next-generation electro-mechanical and anisotropic opto-electronic nanodevices.

1 Introduction

Since the invention of graphene in 2004,[1] intense research in the field of two-dimensional (2D) nanostructures has been carried out by both theoretical and experimental studies.[2–5] 2D layered-structures, such as silicene,[6] germanene,[2] or metal chalcogenide compounds[7] possess many novel physical features that cannot be found in their bulk phases. Among those interesting candidates, group III–VI post-transition metal chalcogenides have appeared recently as a promising family due to their intriguing physical properties.[8,9] Group III metal chalcogenide monolayers can serve as catalysts in photocatalytic applications due to their large band gap and suitable band alignment.[10] With strong absorption of light in the UV-visible region, group III metal chalcogenide are expected to be suitable for applications in photodetectors.[11]

2D layered nanosheets can stably exist in different polymorphs. For example, both the α and γ phases of germanium monochalcogenides have been experimentally fabricated recently.[12,13] More interestingly, the physical properties of these polymorphs are significantly different from each other.[14,15] Therefore, from our point of view, along with the discovery of new materials, the search for new stable polymorphs of available 2D structures is also a necessary work that deserves attention. This will contribute to clarifying the full picture of these materials. In this manuscript, we study a new phase of 2D aluminum monochalcogenide with C_{2h} space group, namely C_{2h}-AlX (X = S, Se, and Te). We knew that the α phase of group III monochalcogenides MX (M is the group III metal) has been experimentally fabricated and widely theoretically studied.[8,16] While the structure of γ-MX monolayers has a graphene-like hexagonal lattice with non-centrosymmetric D_{3h} space group,[8] the atomic structure of C_{2h}-MX It has lower symmetry with larger unit-cell. It is noted that C_{2h} polymorph of bulk group III monochalcogenide InSe has been fabricated[17] and also experimentally investigated previously.[18] Besides, different polytypes of InSe and also C_{2h} phase of GaS, GaSe, InS, and InSe monolayers have been studied theoretically recently by the first-principles method.[19,20] This supports the expectation that 2D C_{2h}-MX sheets can be synthesized soon in the future.

In this study, we investigate the characteristics of the crystal structure, electronic properties, and fundamental optical features of C_{2h} phase of aluminum monochalcogenide monolayers C_{2h}-AlX (X = S, Se, and Te) using first-principles techniques. The structural stabilities of the studied materials are carefully examined based on the evaluation of cohesive energy, phonon dispersion, and analysis of their elastic constants.

[a]Faculty of Applied Sciences, Ho Chi Minh City University of Technology and Education, Ho Chi Minh City, Vietnam. E-mail: anhtt@hcmute.edu.vn

[b]Institute of Research and Development, Duy Tan University, Da Nang, Vietnam. E-mail: hieunn@duytan.edu.vn

[c]Faculty of Natural Sciences, Duy Tan University, Da Nang, Vietnam

[d]Faculty of Basic Sciences, University of Medicine and Pharmacy, Hue University, Hue, Vietnam

[e]Faculty of Physics, Hanoi National University of Education, Ha Noi, Vietnam

Since the structural stabilities are confirmed, we examine the electronic and optical features of the studied materials. The effects of applied strains and electric field on electronic characteristics of C_{2h}-AlX are also reported in the present paper.

2 Computational method

We perform the first-principles simulations based on the density functional theory (DFT) as implemented in the QUANTUM ESPRESSO package.[21] The projector-augmented wave pseudo-potential method[22] with an energy cutoff of 70 Ry is selected to consider the electronic-ion core interactions. The exchange-correlation functions are approximated by generalized gradient approximation with the Perdew, Burke, and Ernzerhof (PBE) parameterization. Besides, the hybrid functional proposed by Heyd, Scuseria, and Ernzerhof (HSE06)[23] is adopted to correct the bandgaps by using the Vienna *ab initio* simulation package.[24,25] Besides, the corrected DFT-D2 approach suggested by Grimme[26] is also included to consider the van der Waals forces. The Brillouin zone is sampled by ($15 \times 15 \times 1$) k-grid mesh based on the Monkhorst–Pack scheme.[27] The convergence criteria for energy is selected to be 10^{-6} eV. To reduce interactions between periodic images in adjacent cells, we insert a vacuum spacing of 25 Å along the vertical direction of the investigated materials. We evaluate the phonon dispersion through the density functional perturbation approximation.[28] The thermodynamic stability is tested based on *ab initio* molecular dynamics (AIMD) calculations using the NVT ensemble with a $6 \times 6 \times 1$ supercell within 8 ps (time step of 1 fs).[29] Born's criterion is used to confirm mechanical stability through the evaluation of elastic coefficients.[30] We used a biaxial strain and external electric field to turn bandgaps of the studied monolayers. The electric field is applied perpendicularly to the 2D plane of the material with the positive direction of the electric field along the z-axis.

3 Calculated results and discussion

3.1 Crystal structure and structural stability

We first optimized the structures of binary AlX (X = S, Se, Te). Apart from previous studies[8] in which the geometry of group III monochalcogenides AlX belong to D_{3h} point group, the current polymorph of AlX monolayers possess the geometry of monoclinic lamellae phase with respect to C_{2h} point group. Fig. 1 presents the atomic structures AlX monolayers viewed along a and b directions in which the unit cell contains eight atoms. It also can be seen that in C_{2h} point group, there are four sublayers X–Al–Al–X held together with polar covalent bonds.

The fully optimized lattice constants are predicted by the Quantum Espresso package and tabulated in Table 1. The lattice parameters a and b increase in the order of AlS, AlSe, and AlTe, namely, their structural parameters increase with increasing the atomic radius of the chalcogen atoms. The trend of two lattice parameters a and b are attributed to the bond lengths of Al–Al and Al–X in the interlayers and intralayers of these lamellae. However, there are neither theoretical nor experimental results related to the C_{2h}-AlX monolayers so far.
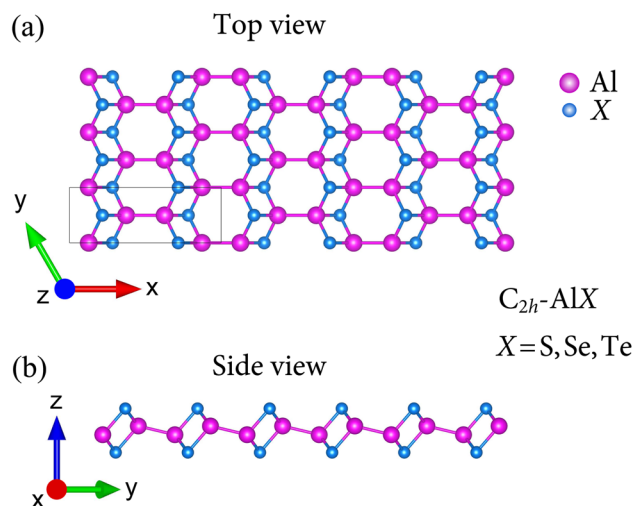

Fig. 1 Crystal structures in top view (a) and side view (b) of C_{2h} phase of AlX (X = S, Se, Te).

Table 1 Lattice constants a and b (Å), monolayer thickness Δh (Å), cohesive energy E_{coh} (eV per atom), and elastic stiffness constants C_{ij} (N m^{-1}) of monolayers C_{2h} AlX

	a	b	Δh	E_{coh}	C_{11}	C_{12}	C_{22}	C_{66}
AlS	9.80	3.57	2.97	−4.86	48.11	3.85	48.38	10.62
AlSe	9.94	3.75	3.24	−4.41	38.54	2.96	45.14	8.40
AlTe	10.10	4.06	3.64	−3.91	23.90	1.75	40.09	4.72

Hence, in order to have a qualitative explanation, the obtained bond lengths of In–X[8] are used and similar trends for lattice parameters are found. The monolayer thicknesses Δh are also calculated and increase when moving down a group. These reasonable results are expected since the monolayer thicknesses are proportional to both Al–Al and Al–X. It is noted that the atomic structure of C_{2h}-AlX exhibits high directionally anisotropic along the armchair and zigzag axes with the anisotropic ratio $\tau = a/b$ up to 2.75 (for AlS monolayer).

In order to investigate the stability of the crystal structure of these proposed systems AlX, we next test the strength of chemical bonding based on the evaluation of cohesive energies, as defined as

$$E_{coh} = \frac{N_{Al}E_{Al} + N_X E_X - E_{tot}}{N_{Al} + N_X}, \quad (1)$$

where E_{tot} indicates the total energy of AlX sheet; E_{Al} and E_X refer to the single-atom energies Al and X, respectively; and N_{Al} and N_X are respectively number of atoms Al and X in the unitcell. The examined results for the cohesive energy per atom for AlX monolayers listed in Table 1 are all negative and hence confirm their thermodynamic stability during the formation of these three structures. The cohesive energies are increasing when going down in this group (S, Se, and Te). The highest energetically stability is observed for the AlS structure (−4.86 eV per atom) and the lowest is observed for the AlTe structure (−3.91 eV per atom). Therefore, the reactivity of the AlTe monolayer towards the
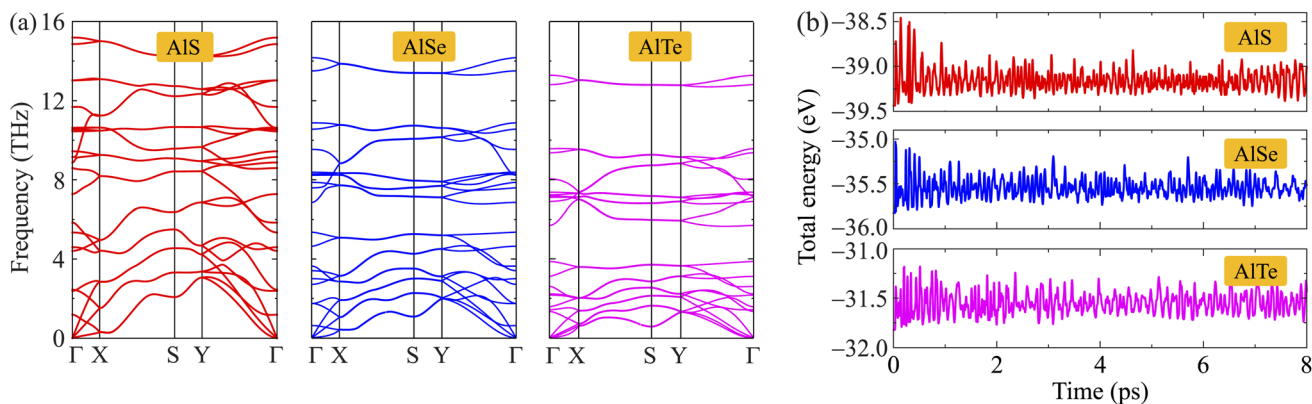
Fig. 2 Phonon dispersions (a) and AIMD calculations for energy fluctuations to time (b) of C_{2h}-AlX monolayers.

other systems is high, followed by that of AlSe and AlS. The obtained results for the cohesive energy of C_{2h}-AlX are comparable with the available D_{3h}-AlX.[8] Previously, Hu and co-workers revealed that there is no significant difference in cohesive energy between D_{3h}-InX and C_{2h}-InX monolayers.[20]

Additionally, to examine the dynamical stabilities of AlX monolayers, the phonon dispersions along the high symmetry line Γ–X–S–Y–Γ are investigated and shown in Fig. 2(a). It is found that the phonon dispersion of AlX monolayers contains 24 vibrational branches due to the unit-cell containing eight atoms as depicted in Fig. 1(a). The phonon spectrum contains three acoustic branches and 21 optical branches. No negative frequencies are available in the whole Brillouin zones that confirm the dynamically stable characteristic of these AlX structures. Besides, the AIMD calculations for the energy fluctuation to time of AlX materials are carried out as shown in Fig. 2(b). Obtained calculations demonstrate that the fluctuations of the total energy of the studied materials are small, only about 0.5 eV. The chemical bonds in all structures are still robust and no significant structural transitions occur during the 8 ps AIMD simulation, suggesting the thermodynamic stabilities of AlX monolayers.

$$Y_{2D}(\varphi) = \frac{C_{11}C_{22} - C_{12}^2}{C_{11}\sin^4\varphi + C_{22}\cos^4\varphi - (2C_{12} - \Lambda)\sin^2\varphi\cos^2\varphi}, \quad (2)$$

$$v(\varphi) = \frac{C_{12}(\sin^4\varphi + \cos^4\varphi) - (C_{11} + C_{22} - \Lambda)\sin^2\varphi\cos^2\varphi}{C_{11}\sin^4\varphi + C_{22}\cos^4\varphi - (2C_{12} - \Lambda)\sin^2\varphi\cos^2\varphi}, \quad (3)$$

where $\Lambda = \dfrac{C_{11}C_{22} - C_{12}^2}{C_{66}}$ and φ is determined by the angle between the x axis and considered direction.

We first calculate the elastic constants C_{ij} of the studied 2D structures based on the fitting in the polynomial function of their uniaxial strain-dependent energy.[33] There are four constants, including C_{11}, C_{22}, C_{12}, and C_{66} (using Voigt's notation), that need to be evaluated for 2D materials. The evaluated results for the C_{ij} of the C_{2h}-AlX are listed in Table 1. It is found that C_{2h}-AlX monolayers exhibit small stiffness constants. All four stiffness constants share a common trend of change, that the C_{ij} decreases with the increasing of the atomic size of the chalcogen element. This is consistent with the statement that

the smaller the lattice constant, the greater the in-plane stiffness.[8] Importantly, the elastic constants listed in Table 1 satisfy the corresponding criteria for elastic stability according to Born–Huang's lattice dynamical theory ($C_{11}C_{12} - C_{12}^2 > 0$, $C_{11} > 0$, $C_{22} > 0$, $C_{66} > 0$).[34] These calculated results suggest that all three C_{2h}-AlX monolayers are mechanically stable.

Due to the anisotropy in the atomic structure, the elastic characteristics of the investigated materials will also be
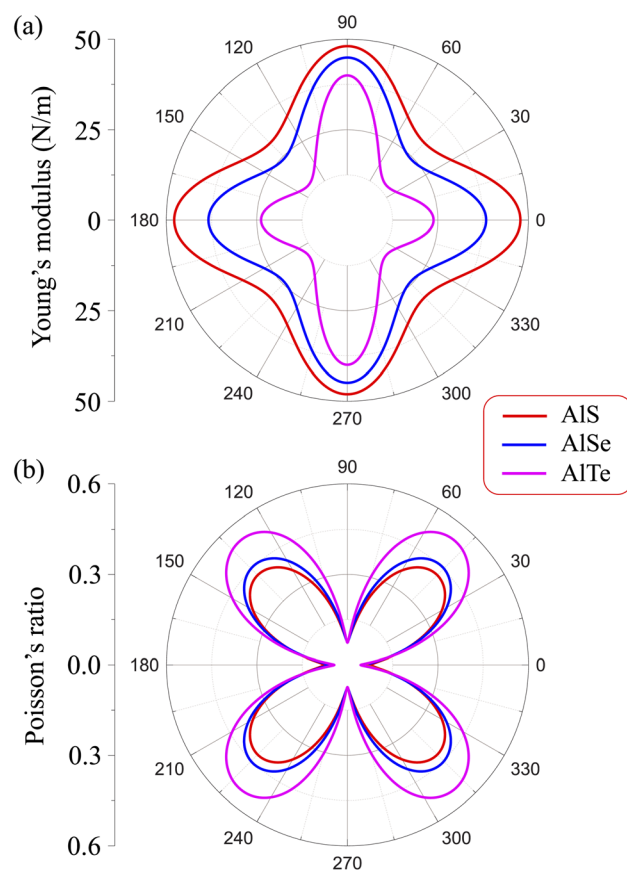

Fig. 3 Dependence of (a) Young's modulus and (b) Poisson's ratio on angular φ of C_{2h}-AlX m0-dependent $Y_{2D}(\varphi)$ and Poisson's ratio $v(\varphi)$ are expressed as follows.[31,32]

anisotropic accordingly. The directional dependent $Y_{2D}(\varphi)$ and $\nu(\varphi)$ of C_{2h}-AlX structures are presented in Fig. 3. At first glance, it is revealed the AlX lamella have strong mechanical anisotropy since both Y_{2D} and ν are changed with different in-plane angles. These results are in good agreement with the anisotropy of the structure of these AlX monolayers. From Fig. 1, we can see that $Y_{2D}(\varphi)$ of C_{2h}-AlX structures depends strongly on the investigated direction, namely the in-plane angle φ. It is calculated that Young's modulus gets the maximum value corresponding to $\varphi = 90°$. The maximum value of Young's modulus $Y_{2D}(90°)$ is evaluated to be 48.07, 44.91, and 39.97 N m^{-1} for AlS, AlSe, and AlTe, respectively. The Young's modulus along the [100] direction ($\varphi = 0°$) is also large, especially in the case of AlS (47.80 N m^{-1}). However, the difference in $Y_{2D}(\varphi)$ along $\varphi = 0°$ and $\varphi = 90°$ directions is progressively larger with increasing atomic radii of the chalcogen elements. At $\varphi = 0°$, Young's modulus of AlTe is only 23.82 N m^{-1}, which is much smaller than that along the $\varphi = 90°$ direction as above-mentioned. From Fig. 3, we found that the C_{2h}-AlX material was the softest along the $\varphi = 45°$ or $\varphi = 135°$ directions with Young's modulus of 30.18, 24.38, and 14.58 N m^{-1} for AlS, AlSe, and AlTe, respectively. Young's modulus of the AlTe monolayer is found to be the smallest, indicating that the AlTe monolayer is the most stretchable, flexible, and promising for flexible material applications. Besides, when going down in this group (S, Se, and Te), Poisson's ratio is increasing, *i.e.*, that of laminated AlTe is the highest, hence, AlTe monolayer has the lowest in-plane stiffness. This result is in accordance with the obtained result of Young's modulus mentioned above and could be attributed to the highest lattice parameters of AlTe (Table 1) in which the bonding between elemental sites becomes weaker. The polar diagram of Poisson's ratio of the studied monolayers is also shown in Fig. 3(b), which provides us with the dependence of the Poisson's ratio on the investigated direction in the 2D plane of the material.

3.2 Electronic properties

The structural and dynamical stabilities are confirmed. Next, the electronic structures are considered by investigating the electronic band dispersions along the high symmetry line Γ–X–S–Y–Γ. Since the DFT techniques parameterized the PBE often underestimate the bandgap, additionally, the HSE06 method is used to correct the band diagram and overcome the underestimation of the bandgap issue. The examined PBE and HSE06 bandgaps for C_{2h}-AlX monolayers are presented in Fig. 3. It can be seen that these three monolayers exhibit semiconducting characteristics with direct band gap energies due to the

alignment of the conduction band minimums (CBM) and the valence band maximums (VBM) at Γ point. The band gap energies obtained by the PBE and HSE06 functionals are tabulated in Table 2. As predicted, the energy gap in the PBE level of C_{2h}-AlX is narrower than that in the HSE06 level. The band gaps are decreasing in order of AlS, AlSe, and AlTe in both PBE and HSE06 functionals calculations. It is also noted that D_{3h}-AlX is an indirect semiconducting material[8] with a wider energy gap compared with corresponding C_{2h}-AlX.

To analyze the formation of electronic bands, we calculate the weighted bands of AlX as shown in Fig. 5. It is found that the VBM of AlX is mainly dominated by the p orbitals of the chalcogen element X. Meanwhile, both X-s and Al-p orbitals have significant contributions to the CBM. Besides, the contribution of the Al-s orbitals to the conduction band is significant.
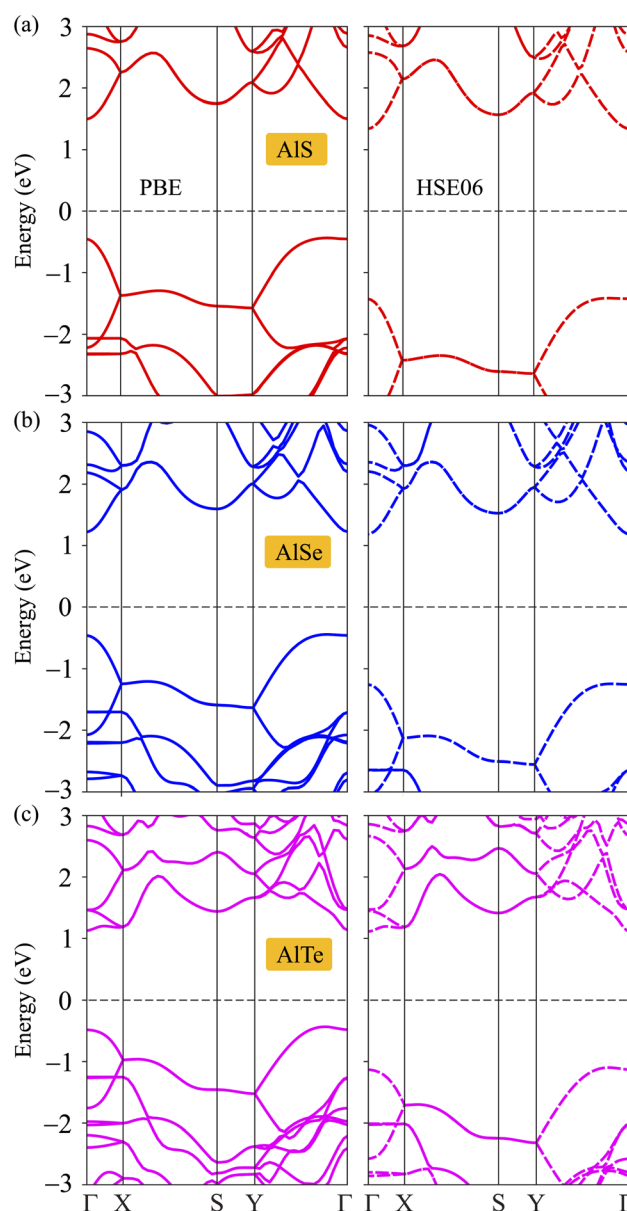

Fig. 4 Calculated band dispersions of monolayers AlS (a), AlSe (b), and AlTe (c) using PBE/HSE06 functional.

Table 2 Band energy gaps calculated by the PBE and HSE06 functionals E_g, Fermi level E_F, vacuum level E_{vac}, and work function Φ of monolayers AlX (X = S, Se, and Te). All parameters are measured in eV

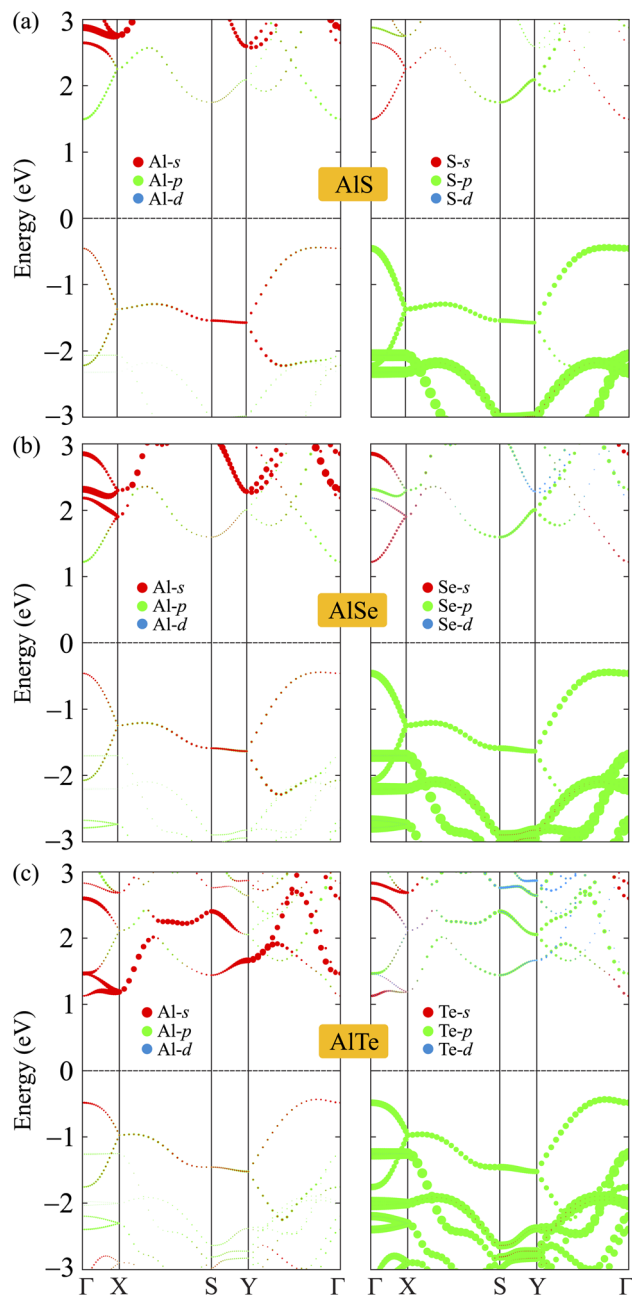|	E_g^{PBE}	E_g^{HSE06}	E_F	E_{vac}	Φ
AlS	1.94	2.75	−3.25	2.12	5.37
AlSe	1.66	2.43	−3.00	2.07	5.07
AlTe	1.56	2.21	−2.20	2.55	4.75

Fig. 5   Weighted bands of monolayers AlS (a), AlSe (b), and AlTe (c) at the PBE level.

Next, we evaluate the ability of the electrons to escape from the surface by calculating the work function of the materials. The work function Φ of materials can be evaluated from the vacuum level Φ_{vac} and Fermi level Φ_{F} as follows:

$$\Phi = \Phi_{\mathrm{vac}} - \Phi_{\mathrm{F}} \qquad (4)$$

The values of Φ_{vac} and Φ_{F} can be obtained based on the analysis of the electrostatic potentials of materials as presented in Fig. 6. Monolayers AlX have vertical symmetric structures, therefore, there is no vacuum level difference between the sides. Obtained results for Φ_{vac}, Φ_{F}, and corresponding Φ are

presented in Table 2. It is found that the AlTe has the smallest work function being 4.75 eV, implying that the electrons can more easily escape from the surface of AlTe than other structures.

Finding ways to modulate physical properties, especially electronic characteristics, has always been a topic of interest to the scientific community. Several methods for modifying electronic properties have been introduced, including doping,[35] placing materials on semiconductor substrates or forming heterostructures,[36,37] surface functionalization,[38] *etc.* Recent studies have shown that mechanical strain is one of the simple and effective approaches in tuning the properties of 2D materials.[3,39] Here, we consider the effect of a biaxial strain on the energy band diagrams of C_{2h}-AlX structures at the PBE level. The biaxial strain ε_b is quantitatively introduced as $\varepsilon_b = (l - l_0)/l_0$. Here, l_0 and l are the lengths of the computed cell of C_{2h}-AlX material before and after strain, respectively.

The electronic band dispersions of C_{2h}-AlX under the biaxial strains are depicted in Fig. 7 It is demonstrated that the effect of the strains on the electronic band dispersions of C_{2h}-AlX is significant. While the tensile strain is a significant change in the band gap, the compressive strain tends to change the position of the VBM. From Fig. 7, we can see that, in the presence of the compressive strain, the VBM tends to move away from the Γ point and lies on the $Y\Gamma$ path. It implies that the compressive strain can lead to phase transition from direct-to-indirect bandgap in AlX materials. The dependence of the band gap of AlX on the applied biaxial strains is depicted in Fig. 8(a). It is shown that the energy gap of AlTe decreases rapidly under tensile strain. In the examined range of the strain, the graph showing the strain-dependent energy for AlS and AlSe is quite similar. The energy gap of AlS increases slightly and then tends to decrease in the presence of tensile strain. For AlSe, the strain reduces its energy gap in both the tensile and compression strains. When the biaxial strain is introduced, there is a significant difference in the bandgaps of AlTe and other structures, namely AlS and AlSe. This may be because the lattice constant difference (and also other structural parameters) between AlTe and AlS/AlSe is larger than that between AlS and AlSe monolayers.

In parallel with the investigation of the change in the physical properties of the material when it is deformed, the investigation of the electronic properties of the material in the presence of an electric field is also a concern of scientists. This is due to the practical significance of this problem in the fabrication and design of nanoelectronic devices. When an electric field was introduced, the effective charge polarization in valence/conduction bands will react to the electric field. As a result, the energy of the electrons in the electronic bands can be significantly modulated accordingly. Besides, the electronic characteristics can be changed due to the redistribution of charge in the studied structures. Ke and co-workers recently showed that electric fields can lead to indirect–direct energy gap phase transitions in the hexagonal 2D structure GaSe.[40] Besides, the effects of electric field on electronic characteristics of asymmetric structure group III Ga$_2$SeTe is also significant, especially in the energy gap.[41] In some 2D structures, however, the effect of the external field on the electronic features is
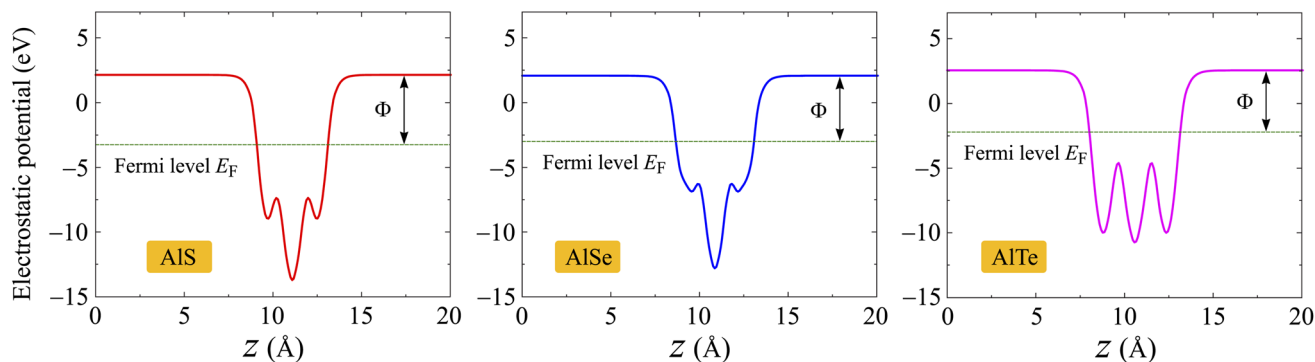
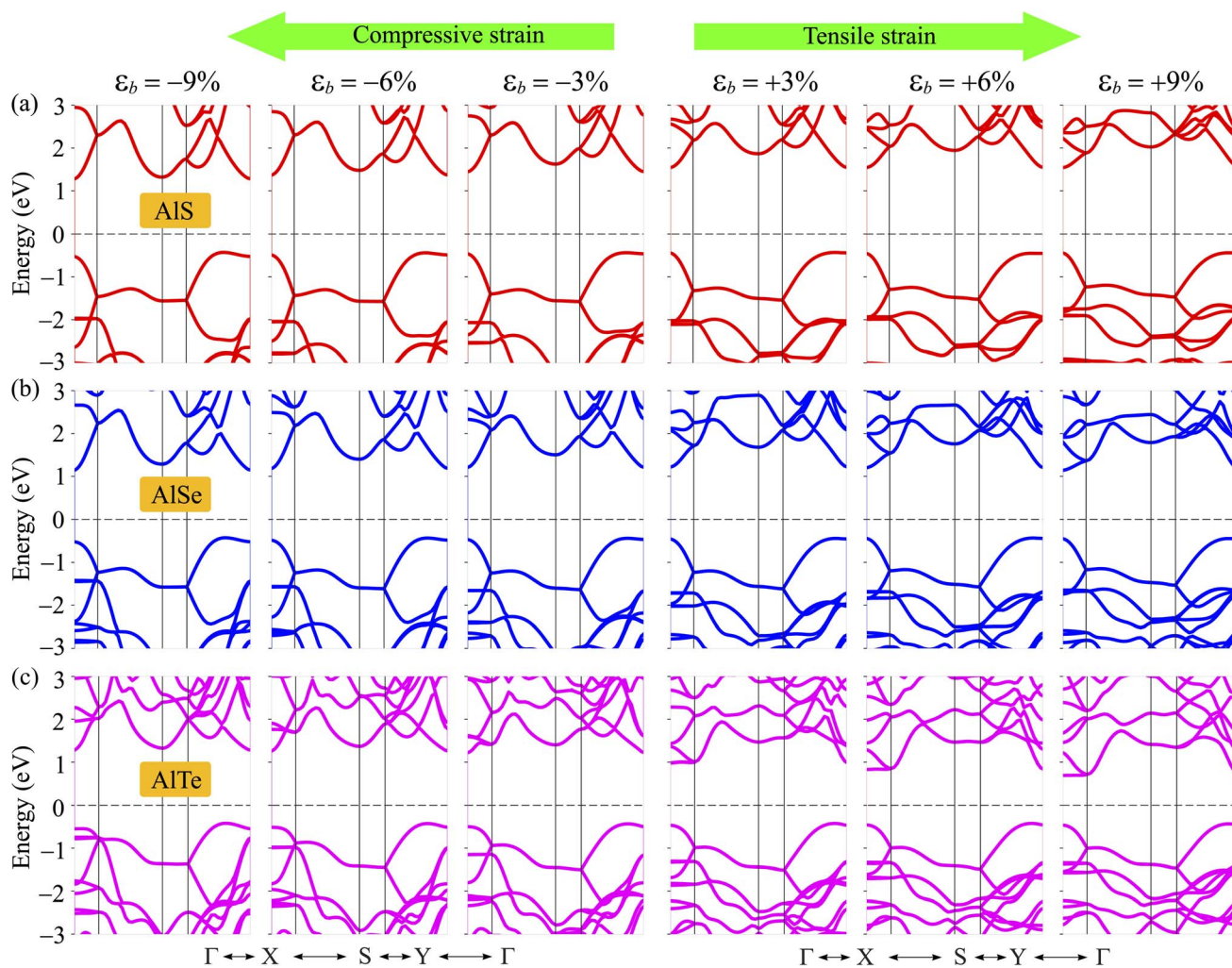Fig. 6   Electrostatic potentials of AlX monolayers. The horizontal dashed line indicates the Fermi level E_F.

Fig. 7   Electronic band dispersions of AlS (a), AlSe (b), and AlTe (c) at several values of ε_b.

insignificant, particularly in the case of the low-applied electric field.[42,43] Wang and co-worker indicated that the energy gap of 2D tellurium structure is almost unchanged under electric fields up to 9 V nm^{-1}.[42] Also, there was no significant change in the energy gap of the γ phase of group IV–VI binary materials when the electric field up to 8 V nm^{-1} was applied.[43] The electronic structures can be significantly altered with the higher applied electric fields. In the present study, we examine the influences of the electric field E on the electronic properties of AlX structures. The field E from 0 to 4 V nm^{-1} is applied perpendicularly to the 2D plane of materials. This value of the electric field is close to that of recent experimental works on 2D structures (3 V nm^{-1}).[44]
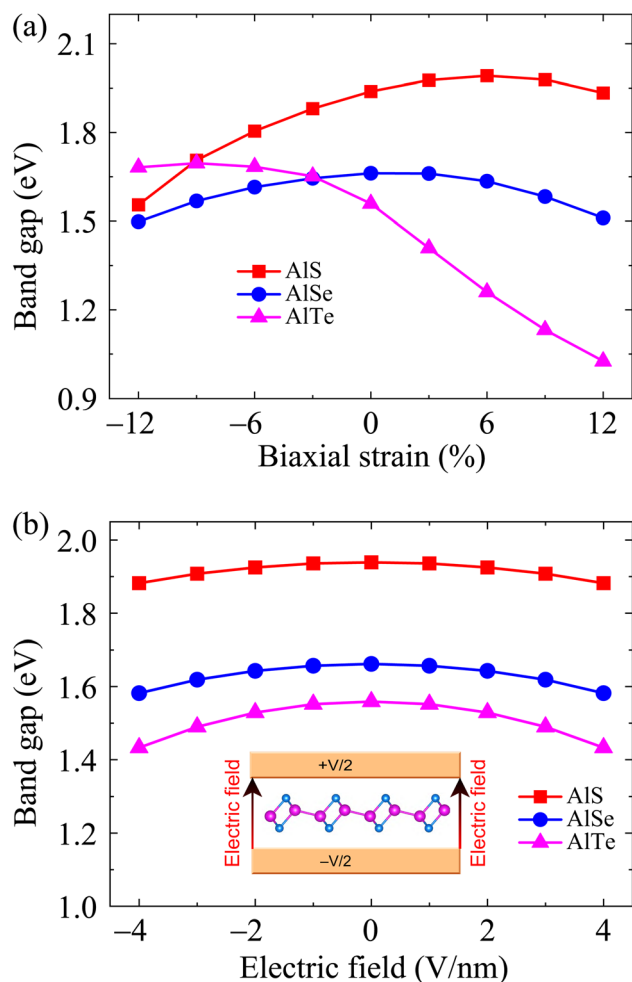
Fig. 8 Dependence of band energy gaps of AlX monolayers on biaxial strain (a) and electric field (b).

where m and e refer to the mass of an electron and elementary charge, respectively; V is the volume of the unit-cell; p indicates the operator of the momentum; f_{kn} denotes the Fermi distribution function, and $|knp>$ stands for the wave function.

We here calculate the optical spectra with the electric field along the crystallographic axes, namely parallel to the 2D plane x ($E_\parallel^{xx}$ and $E_\parallel^y$) and perpendicular to the 2D plane ($E_\perp^{zz}$), corresponding to the electric field vector polarized along the three principal axes x, y, and z. We can evaluate the absorption spectrum $A(\omega)$ based on the calculated dielectric constant parts as follows:[47]

$$A(\omega) = \frac{\sqrt{2}\omega}{c}\left[\sqrt{\varepsilon_1(\omega)^2 + \varepsilon_2(\omega)^2} - \varepsilon_1(\omega)\right]^{1/2} \qquad (6)$$

The optical spectra, including $\varepsilon_2(\omega)$ and $A(\omega)$, are closely related to the band structures of the investigated materials. In the
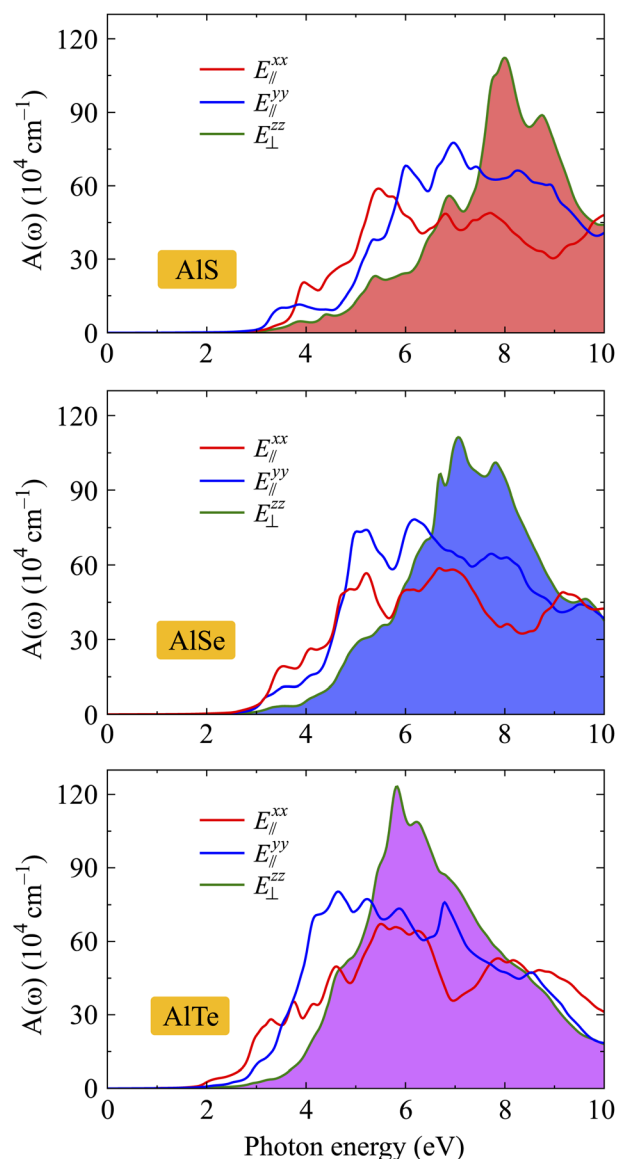

Fig. 9 Dependence of band energy gaps of AlX monolayers on biaxial strain (a) and electric field (b).

Our calculated results demonstrate that the influences of E on the electronic characteristics of the C_{2h}-AlX is insignificant. No significant change in the band diagrams of AlX monolayers when E up to 4 V nm^{-1} is applied (not shown). The dependence of the band gap on the applied electric field is shown in Fig. 8(b). It is observed that the band gap of AlX is only slightly reduced by about 3–8% when the electric field is introduced.

3.3 Optical properties

The basic optical features of material can be described *via* its photon frequency-dependence of the dielectric constant $\varepsilon(\omega)$ written as $\varepsilon(\omega) = \varepsilon_1(\omega) + i\varepsilon_2(\omega)$. It is well-known that we usually calculated $\varepsilon_2(\omega)$ first by summing the filled–empty state transitions and $\varepsilon_1(\omega)$ can be delivered later *via* Kramers–Kronig relationship.[45,46] The imaginary part $\varepsilon_2(\omega)$ is given by:[45,46]

$$\varepsilon_2(\omega) = \frac{4\pi^2 e^2}{Vm^2\varpi^2}\sum_{nn'\sigma}\langle kn\sigma|p_i|kn'\sigma\rangle\langle kn'\sigma|p_j|kn\sigma\rangle$$
$$\times f_{kn}\left(1 - f_{kn'}\right)\delta\left(E_{kn'} - E_{kn} - \hbar\omega\right), \qquad (5)$$

optical spectra, the basic peaks can be explained based on the interband transitions that cause these peaks. The absorption spectra $A(\omega)$ of AlX are depicted in Fig. 9. It is found that the absorption spectra of AlX structures are all activated in the visible light domain which is consistent with their direct energy gaps as presented in Fig. 4. Focusing on the absorption spectrum of each investigated structure, we can see that the absorption coefficient of AlX exhibits strong anisotropy in different polarization directions of the electric field. This is due to the anisotropy in the atomic structure of the investigated structures. In the low photon energy domain, the absorption coefficient in the cases of $E_\parallel^{xx}$ and $E_\parallel^{y}$ is slightly larger than in the case of $E_\perp^{zz}$. However, in the higher photon energy domain, the absorption coefficient in the case of $E_\perp^{zz}$ increases rapidly and reaches its maximum value. From Fig. 9, it is revealed that the main peak of AlS for $E_\perp^{zz}$ is located at 7.99 eV with the value of $A(\omega)$ up to 112×10^4 cm^{-1}. With high absorption, the monolayers AlX are suitable for optoelectronic device applications.

4 Conclusion

In conclusion, we systematically examined the structural, electronic, and optical properties of C_{2h} phase of aluminum monochalcogenides AlX using the DFT simulations. The obtained results indicated that C_{2h}-AlX materials are structurally stable. Unlike the available D_{3h}-AlX structures (indirect semiconductors), C_{2h} phase of aluminum monochalcogenides AlX are semiconductors with direct band energy gap with the HSE06 energy gap values from 2.21 to 2.75 eV. The band gaps of C_{2h}-AlX depend strongly on the applied strain, especially tensile strain. Also, the phase transition from the direct band gap to the indirect band gap was found in C_{2h}-AlX when the compressive strain was introduced. The mechanical and optical properties exhibit marked anisotropy due to the monolayers having an anisotropic atomic structure. Our calculated results indicated that C_{2h}-AlX possesses many novel characteristics that do not exist in other polymorphs of aluminum monochalcogenides. These findings support the view that in parallel with the efforts on the discovery of new materials, the search for new polymorphs of existing nanomaterials is also an approach that needs more attention.

Conflicts of interest

There are no conflicts of interest to declare.

Acknowledgements

References

1 K. S. Novoselov, A. K. Geim, S. V. Morozov, D. Jiang, Y. Zhang, S. V. Dubonos, I. V. Grigorieva and A. A. Firsov, *Science*, 2004, **306**, 666.

2 A. Acun, L. Zhang, P. Bampoulis, M. Farmanbar, A. van Houselt, A. N. Rudenko, M. Lingenfelder, G. Brocks, B. Poelsema, M. I. Katsnelson and H. J. W. Zandvliet, *J. Phys.: Condens. Matter.*, 2015, **27**, 443002.

3 T. V. Vu, C. V. Nguyen, H. V. Phuc, A. A. Lavrentyev, O. Y. Khyzhun, N. V. Hieu, M. M. Obeid, D. P. Rai, H. D. Tong and N. N. Hieu, *Phys. Rev. B*, 2021, **103**, 085422.

4 N. D. Hien, C. V. Nguyen, N. N. Hieu, S. S. Kubakaddi, C. A. Duque, M. E. Mora-Ramos, L. Dinh, T. N. Bich and H. V. Phuc, *Phys. Rev. B*, 2020, **101**, 045424.

5 D. Muoi, N. N. Hieu, C. V. Nguyen, B. D. Hoi, H. V. Nguyen, N. D. Hien, N. A. Poklonski, S. S. Kubakaddi and H. V. Phuc, *Phys. Rev. B*, 2020, **101**, 205408.

6 B. Lalmi, H. Oughaddou, H. Enriquez, A. Kara, S. Vizzini, B. Ealet and B. Aufray, *Appl. Phys. Lett.*, 2010, **97**, 223109.

7 H. S. S. Ramakrishna Matte, A. Gomathi, A. K. Manna, D. J. Late, R. Datta, S. K. Pati and C. N. R. Rao, *Angew. Chem., Int. Ed.*, 2010, **49**, 4059–4062.

8 S. Demirci, N. Avazli, E. Durgun and S. Cahangirov, *Phys. Rev. B*, 2017, **95**, 115409.

9 N. N. Hieu, H. V. Phuc, A. I. Kartamyshev and T. V. Vu, *Phys. Rev. B*, 2022, **105**, 075402.

10 H. L. Zhuang and R. G. Hennig, *Chem. Mater.*, 2013, **25**, 3232.

11 P. Hu, Z. Wen, L. Wang, P. Tan and K. Xiao, *ACS Nano*, 2012, **6**, 5988.

12 D. D. Vaughn, R. J. Patel, M. A. Hickner and R. E. Schaak, *J. Am. Chem. Soc.*, 2010, **132**, 15170.

13 S. Lee, J.-E. Jung, H. gyu Kim, Y. Lee, J. M. Park, J. Jang, S. Yoon, A. Ghosh, M. Kim, J. Kim, W. Na, J. Kim, H. J. Choi, H. Cheong and K. Kim, *Nano Lett.*, 2021, **21**, 4305–4313.

14 N. Luo, W. Duan, B. I. Yakobson and X. Zou, *Adv. Funct. Mater.*, 2020, **30**, 2000533.

15 T. V. Vu, H. V. Phuc, A. I. Kartamyshev and N. N. Hieu, *Appl. Phys. Lett.*, 2023, **122**, 061601.

16 S. Acharya, M. Dutta, S. Sarkar, D. Basak, S. Chakraborty and N. Pradhan, *Chem. Mater.*, 2012, **24**, 1779–1785.

17 G. Vezzoli, *Mater. Res. Bull.*, 1971, **6**, 1201–1204.

18 D. Errandonea, D. Martínez-García, A. Segura, A. Chevy, G. Tobias, E. Canadell and P. Ordejon, *Phys. Rev. B: Condens. Matter Mater. Phys.*, 2006, **73**, 235202.

19 L. Ghalouci, F. Taibi, F. Ghalouci and M. Bensaid, *Comput. Mater. Sci.*, 2016, **124**, 62–77.

20 T. Hu, C. Xu, A. Zhang and P. Yu, *Mater. Adv.*, 2022, **3**, 2213–2221.

21 P. Giannozzi, S. Baroni, N. Bonini, M. Calandra, R. Car, C. Cavazzoni, D. Ceresoli, G. L. Chiarotti, M. Cococcioni, I. Dabo, A. D. Corso, S. de Gironcoli, S. Fabris, G. Fratesi, R. Gebauer, U. Gerstmann, C. Gougoussis, A. Kokalj, M. Lazzeri, L. Martin-Samos, N. Marzari, F. Mauri, R. Mazzarello, S. Paolini, A. Pasquarello, L. Paulatto, C. Sbraccia, S. Scandolo, G. Sclauzero, A. P. Seitsonen, A. Smogunov, P. Umari and R. M. Wentzcovitch, *J. Phys.: Condens. Matter*, 2009, **21**, 395502.

22 P. E. Blöchl, *Phys. Rev. B: Condens. Matter Mater. Phys.*, 1994, **50**, 17953–17979.

23 J. Heyd, G. E. Scuseria and M. Ernzerhof, *J. Chem. Phys.*, 2003, **118**, 8207.

24 G. Kresse and J. Furthmüller, *Phys. Rev. B*, 1996, **54**, 11169–11186.

25 G. Kresse and J. Furthmüller, *Comput. Mater. Sci.*, 1996, **6**, 15–50.

26 S. Grimme, *J. Comput. Chem.*, 2006, **27**, 1787.

27 H. J. Monkhorst and J. D. Pack, *Phys. Rev. B: Condens. Matter Mater. Phys.*, 1976, **13**, 5188–5192.

28 T. Sohier, M. Calandra and F. Mauri, *Phys. Rev. B*, 2017, **96**, 075448.

29 S. Nosé, *J. Chem. Phys.*, 1984, **81**, 511.

30 M. Born and K. Huang, *Am. J. Phys.*, 1955, **23**, 474.

31 N. T. Hung, A. R. T. Nugraha and R. Saito, *J. Phys. D: Appl. Phys.*, 2018, **51**, 075306.

32 P. Xiang, S. Sharma, Z. M. Wang, J. Wu and U. Schwingenschlögl, *ACS Appl. Mater. Interfaces*, 2020, **12**, 30731.

33 K.-A. N. Duerloo, M. T. Ong and E. J. Reed, *J. Phys. Chem. Lett.*, 2012, **3**, 2871–2876.

34 F. Mouhat and F.-X. Coudert, *Phys. Rev. B: Condens. Matter Mater. Phys.*, 2014, **90**, 224104.

35 Y.-C. Lin, J. Karthikeyan, Y.-P. Chang, S. Li, S. Kretschmer, H.-P. Komsa, P.-W. Chiu, A. V. Krasheninnikov and K. Suenaga, *Adv. Mater.*, 2021, **33**, 2007819.

36 H. V. Phuc, N. N. Hieu, B. D. Hoi, L. T. T. Phuong and C. V. Nguyen, *Surf. Sci.*, 2018, **668**, 23–28.

37 C. V. Nguyen, M. Idrees, H. V. Phuc, N. N. Hieu, N. T. T. Binh, B. Amin and T. V. Vu, *Phys. Rev. B*, 2020, **101**, 235419.

38 V. T. T. Vi, C. Q. Nguyen, B. D. Hoi, H. V. Phuc, C. V. Nguyen and N. N. Hieu, *J. Phys. D: Appl. Phys.*, 2022, **55**, 505302.

39 T. V. Vu, V. T. T. Vi, H. V. Phuc, C. V. Nguyen, N. A. Poklonski, C. A. Duque, D. P. Rai, B. D. Hoi and N. N. Hieu, *J. Phys.: Conden. Matter*, 2021, **33**, 225503.

40 C. Ke, Y. Wu, G.-Y. Guo, W. Lin, Z. Wu, C. Zhou and J. Kang, *Phys. Rev. Appl.*, 2018, **9**, 044029.

41 T. V. Vu, V. T. T. Vi, C. V. Nguyen, H. V. Phuc and N. N. Hieu, *J. Phys. D: Appl. Phys.*, 2020, **53**, 455302.

42 J. Wang, H. Shen, Z. Yu, S. Wang, Y.-Y. Chen, B.-R. Wu and W.-S. Su, *ACS Omega*, 2020, **5**, 18213–18217.

43 V. V. Thanh, N. D. Van, D. V. Truong and N. T. Hung, *Appl. Surf. Sci.*, 2022, **582**, 152321.

44 K. F. Mak, C. H. Lui, J. Shan and T. F. Heinz, *Phys. Rev. Lett.*, 2009, **102**, 256405.

45 A. Delin, P. Ravindran, O. Eriksson and J. Wills, *Int. J. Quantum Chem.*, 1998, **69**, 349.

46 S. Z. Karazhanov, P. Ravindran, A. Kjekshus, H. Fjellvag and B. G. Svensson, *Phys. Rev. B: Condens. Matter Mater. Phys.*, 2007, **75**, 155104.

47 P. Ravindran, A. Delin, B. Johansson, O. Eriksson and J. M. Wills, *Phys. Rev. B: Condens. Matter Mater. Phys.*, 1999, **59**, 1776–1785.